

Prediction of Bonded Asymmetric Metallic Cross-Tension and Single Lap Shear Joints Using Finite Element Model with Material-Level Adhesive Properties and Cohesive Zone Method

Ahmed H. Ibrahim¹, Brock Watson¹, Hamid Jahed¹, Saeid Rezaee², Christine Royer², Duane S.

Cronin^{1*}

¹*Department of MME, University of Waterloo, 200 University Avenue West, Waterloo,*

Canada

²*Renault Group, Boulogne-Billancourt, France*

Abstract

Predictive finite element (FE) models of adhesive joints are needed to enable the design and evaluation of adhesively joined structures, particularly large-scale structures that may be costly to assess experimentally. Although models calibrated to coupon-level tests have provided an important first-step, models based on material-level characterization are needed to enable joint assessment in complex modes of loading. In the present study, a structural epoxy adhesive was characterized using rigid double cantilever (Mode I) and bonded shear (Mode II) specimens to provide material-level input properties. Three single-lap shear (SLJ) and 7 cross-tension (CT) specimen configurations were fabricated with aluminum and steel sheet materials. The specimens included symmetrical (the same adherend material and thickness) and asymmetrical (dissimilar adherend material or unequal thickness) configurations, with three loading angles (0°, 45°, 90°) for the CT specimens. Finite element models of the SLJ and CT specimens were developed using Cohesive Zone Modelling for the

adhesive, with properties determined from the Mode I and Mode II characterization tests. The FE models of the SLJ and CT test specimens predicted the peak load within an average difference of 2% to 19%. The joint strength varied between different test configurations, owing to adherend deformation, load eccentricity and mixed-mode loading. Importantly, the model parameters were not calibrated to the SLJ and CT tests. The FE models were able to predict joint response for varying test specimen geometry, adherend thickness, adherend material, and modes of loading.

Keywords: finite element modeling, toughened adhesives, mechanical properties of adhesives, cohesive zone model, metals

1. Introduction and Background

Adhesive joining has the potential to facilitate the integration of lightweight materials in structures with enhanced performance and crashworthiness compared to traditional methods such as resistance spot welding [1,2]. The adoption of adhesives in vehicle structures requires developing numerical models to facilitate vehicle structure design and assessment, and reduce costly experimental and prototype testing [2]. To develop adhesive finite element (FE) models, adhesives have been characterized under relevant modes of loading to measure the mechanical properties and modelling parameters [3].

Cohesive zone modelling (CZM) has been used to model adhesive joints and predict their mechanical response including failure. The cohesive relationship, describing the adhesive crack initiation and propagation, has been characterized using fracture and strength tests [3]. For example, to characterize the Mode I response of an adhesive, a double cantilever beam (DCB) test is used to measure the fracture properties (i.e., critical energy release rate), and a butt joint or bulk adhesive tensile test is required to determine other properties, such as tensile strength, and elastic modulus [3,4]. However, the requirement for multiple tests, and complex analysis techniques present challenges for the general characterization of adhesives. Thus, many researchers have calibrated or optimized the CZM parameters to match the adhesive joint mechanical response in relevant coupon-level tests, such as single lap shear or H-shaped specimens [5,6]. Calibrating CZM traction-separation relationship leads to case-specific adhesive FE models that may not apply to joints with complex modes of loading or be extendable to larger-scale models of adhesive joined structures (*e.g.* automotive structure components).

Efforts have been made to reduce the number of tests required to characterize adhesive response and determine the cohesive traction-separation relationship required for adhesive

FE modeling. The rigid double cantilever beam (RDCB) was designed to minimize strain energy storage in the adherends under Mode I loading [7]. The RDCB was applied to toughened structure adhesive, and the analysis was improved to account for the compression stress distribution [8]. Recently, a bonded shear specimen (BSS) has been proposed to address the limitations of the end-notch flexure (ENF) test and measure the traction separation response under Mode II without the need for two independent tests [9]. Without the requirement for additional failure strength testing, the RDCB and BSS tests accurately characterized the traction-separation relationship under Mode I and Mode II loading.

The SLJ test is widely used to investigate adhesive joints, due to the test simplicity and relevance to automotive structures [1,4,10]. SLJ specimens have been used to evaluate the mechanical performance (*i.e.* joint strength and energy absorption) and validate FE models of adhesive joints with metallic and non-metallic adherends [1,11]. The influence of adherend material on SLJ joint strength and mode mixity has been assessed using SLJ FE models incorporating shell elements and CZM method for adherends and adhesive, respectively [1]. The FE models enabled the prediction of SLJ peak load and suggested that adherend material substantially influenced mode mixity. In addition, the optical measurement of SLJ joint rotation was reported to provide good validation of the local kinematics of the FE model [1]. Adhesive joint strength is dependent on adherend thickness and material strength [12,13]. SLJ strength showed strong co-dependence on adherend yield strength and sheet thickness [13]. In materials with low yield strength, increasing the adherend thickness reduced the amount of adherend plastic deformation; while increasing sheet thickness for a material with higher yield strength increased the bending moment and led to a reduction in joint strength [14,15].

Automotive structures experience various modes of loading during service [16]. In the SLJ test, the adhesive layer exhibits varying degrees of mode mixity depending on adherend and adhesive properties (*e.g.*, adherend thickness, adherend material, adhesive flexibility) [1,15]. Thus, several researchers have used cross-tension (CT) tests to assess the mechanical response of adhesive joints under different loading angles [17,18]. The CT joints under Mode I loading can exhibit up to 83% lower strength relative to SLJ tests (10.64 kN for SLJ and 1.77 kN for CT) [18], highlighting the substantial adhesive strength reduction in Mode I and adhesive joint sensitivity to the mode of loading. The ability to directly integrate material-level properties of adhesives into FE models of different tests is currently somewhat limited, which makes it challenging to extend adhesive FE models to large-scale structures. Another aspect that has not been systematically assessed in adhesive FE models with the CZM approach is varying adherend thickness and adherend material under various modes of loading.

In the current study, a structural adhesive was characterized in Mode I (RDCB) and Mode II (BSS) loading to develop traction-separation relationships for a CZM model. Three SLJ and seven CT specimen configurations, made with aluminum and steel alloys, were tested to assess symmetrical and asymmetrical joints at three loading angles (0°, 45°, 90°). FE models of each test specimen were developed, incorporating the material-level properties for the adhesive, and assessed against the experimental tests.

2. Experimental and Numerical Methodology

2.1. Adhesive Characterization in Mode I and Mode II Loading

Mode I and Mode II characterization of a structural one-part epoxy adhesive (BetaGuard CI6125R; PPG, France) was completed using RDCB and BSS specimens (Figure 1), following the

methods of [8,9]. The BSS geometry, based on a concept similar to TAST, was optimized to maximize the second moment of area in the bending direction of the specimen, which confined all the deformations within the adhesive layer [9]. Consequently, the BSS test analysis reduced the complex analysis required to account for adherend deformation and allowed direct measurement of the full traction-separation relationship. Similarly, the RDCB geometry has been optimized to maximize the test specimen rigidity, minimizing the geometrical effects of the adherends [8]. The specimens were machined from 1008 steel alloy with Young's modulus of 207 GPa and yield strength of 345 MPa. The bonding surfaces were degreased prior to grit-blasting with 60-grit aluminum-oxide abrasive media for 10 seconds at 500 kPa. The grit-blasted surfaces were then cleaned using acetone to remove abrasive media residues and contamination. The boundaries of the bonding area were masked to achieve a consistent bonding area of 13.2 x 6.35 mm and 12.7 x 3.18 mm for the RDCB and BSS specimens, respectively.

A continuous bead of adhesive was applied to the bonding area on each adherend and spread using a spatula; then the adherends were mated within curing fixtures [8,9]. The adhesive was cured at 180 °C, for 25 minutes. The excess adhesive was removed after curing using a file and sharp blade, and two reference marks were added to each BSS adherend, adjacent to the bond line, to allow optical tracking and post-test analysis (Figure 1b). Also, the RDCB analysis required measuring the bond line length, and distance between specimen edge and center of loading pin [8] (Figure 1a), which was completed using an Opto-digital microscope (ODM) (VHX 5000; Keyence, Japan).

A hydraulic load frame, controlled using an MTS Flex Test SE controller (MTS, USA), was used to load the specimens, and a 2.2 kN load cell measured the force while a linear variable differential transformer measured the cylinder displacement. The crosshead velocity was

kept constant at 0.025 mm/s and tests were synchronously recorded to optically measure the separation on the test specimen (Figure 1, Tracking Targets). Each test was recorded at 30 fps using a single, digital single-lens reflex (DSLR) camera (Nikon D3200; Tokyo, Japan) at a resolution of 1920 x 1080 pixels. The DSLR was fitted with a 105 mm f2.8 macro lens (Sigma Corporation; Setagaya, Japan) and a 2X teleconverter (Kenko TelePlus PRO 300 2X DGX; Tokyo, Japan) to capture 85-95 pixels/mm, providing accurate displacement measurement within $\pm 5\%$ average relative error. A total of 5 RDCB and 5 BSS specimens were tested and analyzed to characterize the adhesive. The force-displacement responses of the RDCB and BSS tests were used to extract the traction-separation relationships, using the methodology laid out in [8,9].

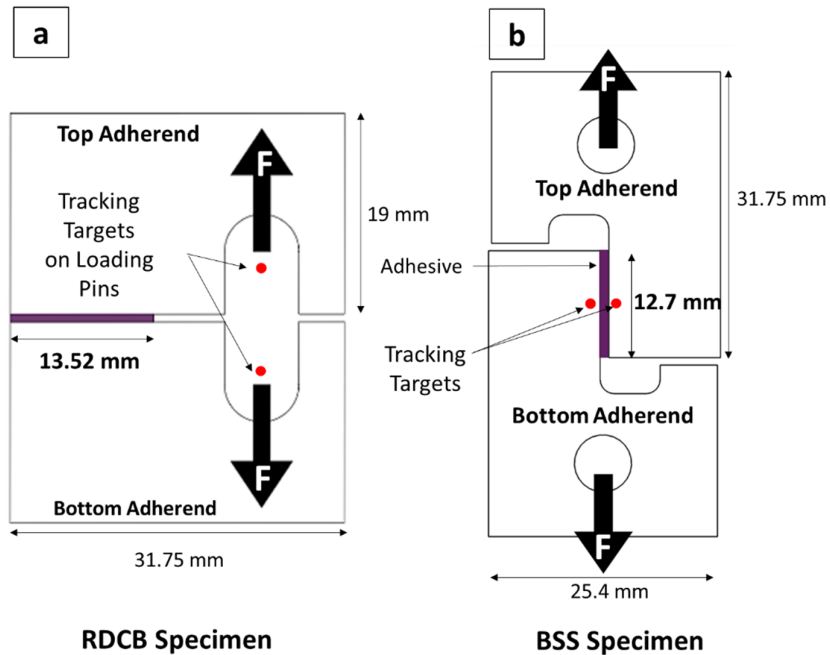


Figure 1. Adhesive characterization specimens for Mode I (RDCB, a) and Mode II (BSS, b). Adapted from [9].

2.2. Preparation and Testing of Adhesive Single Lap Shear (SLJ) and Cross Tension (CT)

Joints

The SLJ and CT specimens were made of adherends 38 mm wide and 125 mm long (Figure 2). The adherend materials (Table 1), were 6000 series Mg-Si aluminum alloy (Al) sheets (1 mm and 2 mm thickness) and a high-strength low-alloy (HSLA) steel sheet (1.5 mm thickness). Ten combinations of adhesive SLS and CT joints were considered while varying adherend material (aluminum and steel), sheet thickness (1, 1.5 and 2 mm) and CT test loading angles (0° for Mode I, 45° for mixed-mode and 90° for Mode II) (Table 2).

Table 1. Adherend material properties.

Adherend Material	Si-Mg Aluminum Alloy (Al)	HSLA Steel
Density (kg/m ³)	2.71	7.8
Young's Modulus, E (GPa)	72	200
Poisson's Ratio	0.33	0.30
Yield Strength, YS (MPa)	150	340

Table 2. Test matrix of SLJ and CT test specimens: Ten conditions showing the number of repeats for each loading angle and adherend configuration.

Test Specimen	Adherend Configuration		
	1 mm Al	1 mm Al	1 mm Al
	1 mm Al	2 mm Al	1.5 mm Steel
SLJ	5	5	5
0° CT	5	5	5
45° CT	5	-	-
90° CT	5	5	5

The aluminum and steel adherends were waterjet cut from sheet material, then degreased using acetone and wiped using a lint-free cloth. The contaminant-free adherends were dipped for 15 seconds in a special coating mixture, of a rust preventive oil (FERROCOTE 6130, Quaker,

USA) and a degreasing solvent (Heptane F), representing an automotive production process. The adherends were slowly removed, then allowed to drip for 30 minutes until a uniform coat of the mixture was observed and the weight of the coating was achieved. The adherends were joined using the same structural one-part epoxy adhesive reported in the characterization and it was important that the adhesive used in this work be formulated to achieve adequate adhesion and cohesive failure when applied to coated surfaces. The bond line length was 12.5 mm [19] and was centred along the overlap length of 37.5 mm. Two Teflon-coated fibreglass spacers (Figure 2, Gap with 0.2 mm spacer) were applied to the joint overlap to achieve a nominal bond line thickness of 0.2 mm and mask the remaining overlap area, avoiding undesirable effects of adhesive spread during adherend mating. A continuous bead of adhesive was applied to the bonding area ($12.5 \pm 0.25 \text{ mm} \times 38 \pm 0.5 \text{ mm}$), and the bead size was identified to ensure proper coverage and avoid the formation of voids.

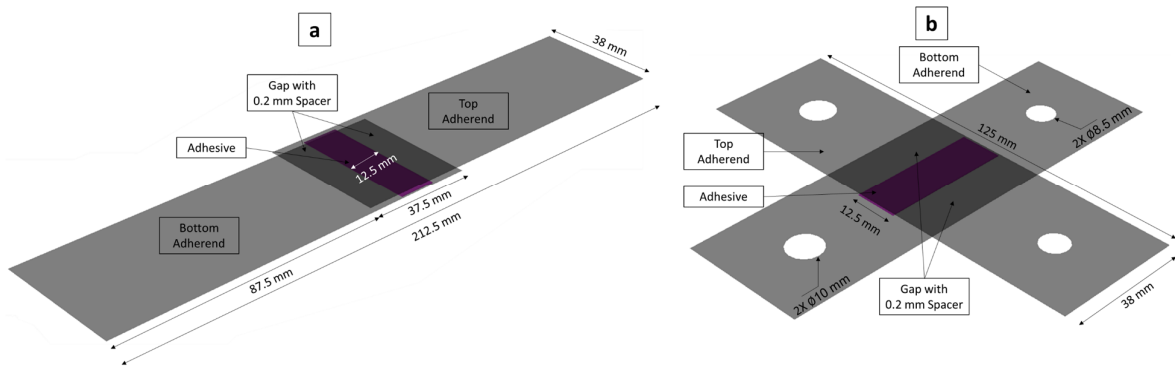


Figure 2. The geometry of the SLJ (a) and CT (b) test specimens. Adherends are shown in grey, adhesive in purple.

SLJ and CT joints were created with Al - Al adherends and Al - steel adherends while varying Al sheet thickness, and five specimens were tested for each combination (Table 2). SLJ samples were assembled in a precisely ground fixturing jig while curing according to the manufacturer's recommendation. CT samples were assembled by stacking the samples in a precisely aligned fixture, comprising a thick bottom plate with four poles and a matching top

plate to apply uniform pressure. The curing fixtures were put in a convection oven to cure the assembled adhesive specimens at 180 °C for 25 minutes (same curing process as the RDCB and BSS specimens). The curing fixtures were designed and used to facilitate preparing test specimens with consistent bond line thickness, bond line length and joint overlap. The excess adhesive was removed, and square tabs (38 mm x 38 mm) were glued to the clamping areas of each test specimen to improve alignment and avoid load eccentricity.

Bond line thickness, bond line length, and joint overlap measurements were carried out on the side of the SLJ samples using an Opto-digital microscope and measurement system (VHX-5000, Keyence, Japan). One of the limitations of CT specimen geometry was that it did not allow for optical measurements of these parameters before testing, so the curing fixture was used to ensure specimen consistency in terms of bond line thickness and adherend alignment. The joint overlap was maintained at 37.95 ± 0.5 mm. The measured bond line thickness of the SLJ specimens had an average of 0.297 ± 0.046 mm. In SLJ and CT specimens, the bond line length was controlled prior to adhesive application and the average bond line length was measured at 12.60 ± 0.10 mm.

The specimens for each configuration were tested in a servo-hydraulic tensile frame (Instron 8892; Instron, USA) with a 25 kN load cell at a crosshead speed of 1 mm/min, corresponding to a nominal strain rate of 0.1 s^{-1} . SLJ testing utilized a 105 mm macro lens to track the joint overlap rotation with a resolution of 66 pixel/mm in the area of interest [1]. SLJ overlap rotation was measured by the change in angle of the line connecting points 'P1' and 'P2' (Figure 4a), which was tracked using software (Tracker, Open Physics Project). The CT specimens required a testing apparatus, which was attached to the testing frame (Figure 4 b, c, d), to eliminate the out-of-plane displacement and control the loading angle. The testing apparatus consisted of a fixed frame with two shafts, and a moving carriage that translates in

one degree of freedom along the shaft using three linear motion bearings (Figure 3). A bar connected to the moving carriage was mounted on the grips of the tensile frame to apply displacement to the CT specimen while measuring the load using the load cell on the frame. The apparatus was made of steel and designed for a maximum load capacity of 20kN at 0°, 45° and 90° loading orientations. Importantly, the apparatus controlled undesirable out-of-plane motion and loading, reporting a negligible lateral deformation of less than 0.01 mm at the maximum load capacity. The different hole diameters on the CT geometry, allowed for precise positioning of the CT specimen within the test specimen holders (Figure 2b). To characterize the force-displacement response of adhesive joints with various loading conditions and adherend combinations, 15 SLJ, 15 0° CT, 5 45° CT, and 15 90° CT specimens were tested.

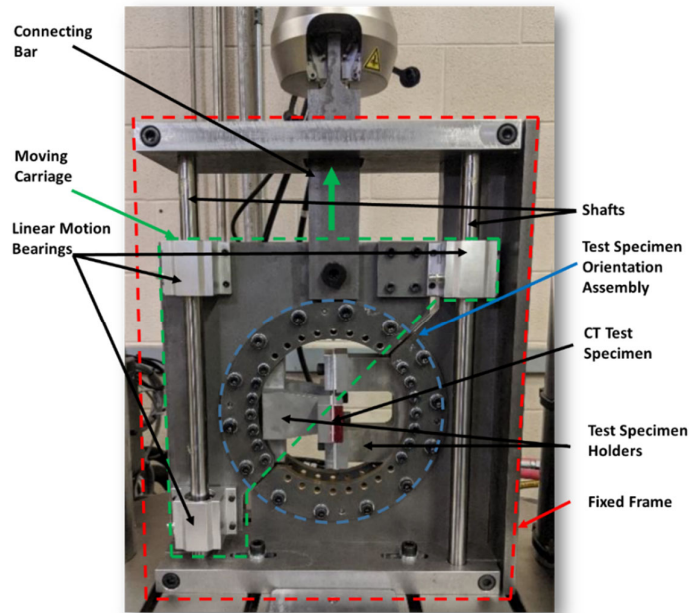


Figure 3. Cross tension testing apparatus allowed changing the loading orientation and minimized lateral deflection.

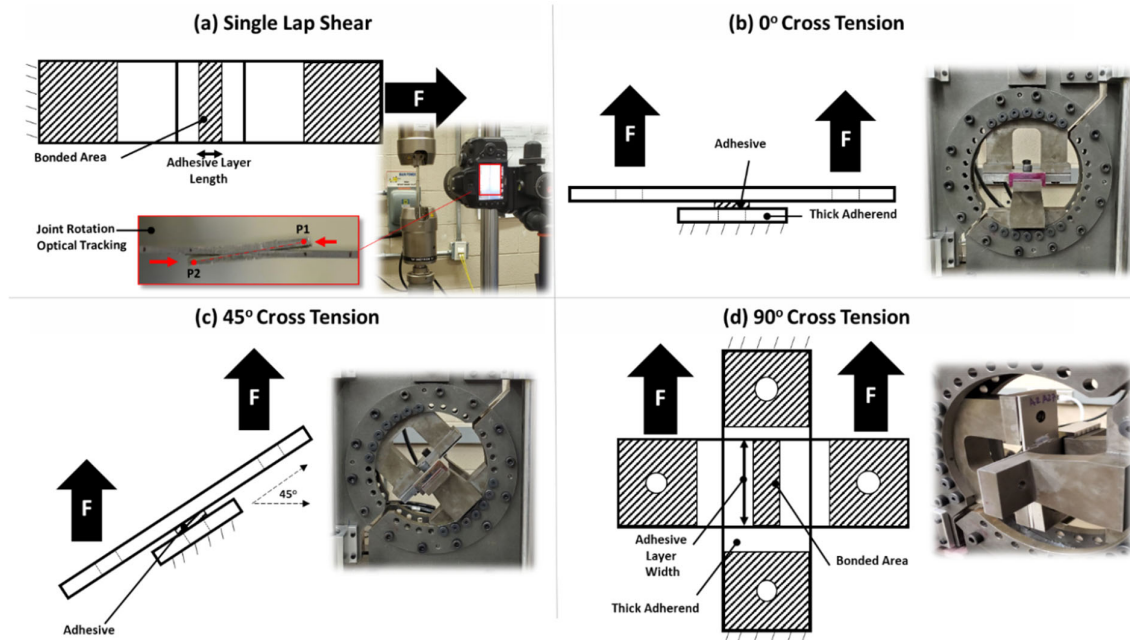


Figure 4. SLJ tests with optical tracking of joint rotation (a), and CT joint tests at 0° (b), 45° (c) and 90° (d) angles. **F** indicates the loading orientation.

2.3. Finite Element Model Development

FE models of the test specimens were developed and solved using a commercial FE package (ABAQUS Standard 2018; Simulia, Dassault Systemes). The three-dimensional models included the nonlinear geometry feature in the software to account for the compliance of the Al adherends, and the out-of-plane response of asymmetrical joints. The models utilized an implicit formulation using a double-precision solver to simulate the quasi-static testing of adhesive joints. Fully integrated four-node, finite membrane strain shell elements (2x2 mm with 5 integration points through thickness) with six degrees of freedom were used to model the adherends (ABAQUS element type S4). These elements were chosen due to their compatibility with structural scale and full-vehicle models and their accuracy in capturing large strains and rotations using a single element through thickness. The shell reference surface was coincident with the mid-surface of the adherend. Both Al and steel adherends were modelled using an elastic-plastic material model with isotropic hardening (post-yield

behaviour defined in ABAQUS *PLASTIC option). The material model parameters (i.e., elastic properties and flow stress-plastic strain data) were obtained from material characterization tensile tests at a quasi-static loading rate. The material models of the adherends did not require a failure criterion because failure occurred within the adhesive joint in all the tests. The adhesive was modeled using eight-node CZM elements with a thickness equal to the measured bond line thickness (section 3.2) and was discretized using 1 mm x 1 mm elements. The mesh size was identified using a mesh sensitivity study, utilizing the guidelines published for the maximum cohesive element size based on the adhesive mechanical properties [20]. The top and bottom surfaces of CZM elements were connected to the adherend shell surfaces using a tie constraint, considering shell thickness and rotational degrees of freedom (Figure 5c). The Mode I and Mode II CZM traction-separation relationships were defined using the characterization results of the RDCB and BSS tests. The shape of the traction-separation relationship can influence the adhesive damage progression and the numerical convergence of the FE solution. Thus, a bilinear (triangular) traction-separation relationship was used because it has been reported to be suitable for adhesives showing brittle to relatively ductile behaviour with limited plastic deformation at joint separation [21,22]. Also, the bilinear relationship is widely available, simple to adopt in FE packages, and has less susceptibility to numerical divergence compared to other shapes of traction-separation relationship (i.e. trapezoidal) [23], which is important for future application in large automotive models. Adhesive damage initiation was defined by a quadratic nominal stress criterion, and damage progression was based on the critical energy release rate (G_c). Adhesive failure associated with mixed-mode loading was governed by the power-law criterion with an exponent (α) of 1 [24,25]. The force data was extracted from the models by monitoring the loads required to maintain the prescribed displacement at the boundaries.

To model the end conditions of the SLJ tests, axial displacement and rotation of the model was fixed at the top and bottom surfaces of the clamping (grip) area at one end (Constrained Grip, Figure 5a). The top and bottom surfaces of the clamped area at the opposite end of the specimen were prescribed a displacement and fixed in the other two translation degrees of freedom (Translating Grip, Figure 5a). The SLJ joint rotation was calculated by extracting the coordinates of the nodes marked with red points (Figure 5a).

To model the end conditions of the CT tests, two reference points were created at the top and bottom of the model and kinematic couplings were defined to link each reference point to the nodes of two grip areas of each adherend (Figure 5b). The CT stiffness response was sensitive to the boundary conditions of the grip areas, and the experimental results showed deformations that extended within the grip areas. Thus, modeling the deformations in these areas was important and facilitated proper prediction of the initial stiffness response. To address this challenge with shell elements, the grip areas were partitioned so that different constraints could be applied to each half of the grip (Figure 5b). For the fixed adherend, half of the grip area was constrained in translation and rotation (Figure 5b, red grip areas), while the other half had the same conditions at the side edges only and allowed longitudinal in-plane deformation (Figure 5b, yellow grip areas with red edges). That allowed in-plane deformation while constraining lateral displacement and rotation around the x and z axes. A similar approach was followed for the loaded adherend with the grip areas allowed to translate in the direction of the applied load (Figure 5b, Translating Grip and Edges). To simulate the test specimen loading, a displacement was applied to the grip areas of the loaded adherend (Figure 5b, orange arrows represent a loading in 0° direction).

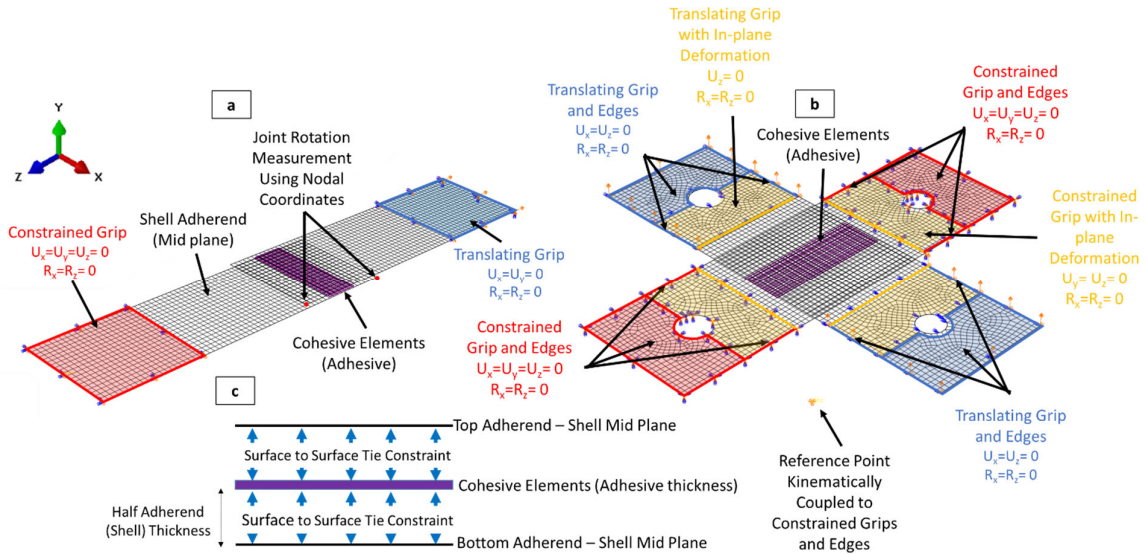


Figure 5. SLJ model (a), CT model (b), and a detailed through-thickness schematic of the adhesive bond line model (c). (U and R represent the colour-coded translation and rotation boundary conditions, respectively)

3. Results and Discussion

3.1. Adhesive Characterization and Cohesive Zone Parameters

The RDCB showed consistent peak traction and displacement at failure (red curves, Figure 6), with average peak traction of 46.82 MPa. The BSS specimens demonstrated peak traction of 33.08 MPa with a plateau and displacement at failure higher than RDCB tests (blue curves, Figure 6), indicating some adhesive ductility in Mode II loading. In all RDCB and BSS tests, the adhesive fracture surface exhibited a cohesive failure, and no interfacial failure was observed. The response of each RDCB and BSS test was fitted to a bilinear response using least-squares fit, determining the stiffness, peak traction, separation at peak traction and separation at failure. The critical energy release rate was calculated by finding the area under each bilinear traction-separation response. The mean value for each CZM parameter was calculated (Table 3) and an average bilinear traction separation response was generated for each mode of loading (Figure 6, Bilinear Fitting).

The RDCB and BSS data analysis and traction-separation fitting approach, developed and reported by Watson et al. [9], was used in the present study to fit the data to a bilinear traction-separation relationship. One of the limitations of the bilinear fitting was the rapid transition from damage initiation to damage progression at the point of peak traction, which did not fully represent the toughening effect along the bond line under Mode II loading (i.e., increased ductility and plateau seen before adhesive failure). This limitation was addressed by fitting the Mode II unloading curve such that the traction-separation response exhibited a separation at failure (critical opening displacement) equal to the average experimental response [26]. Thus, the bilinear fitting represented the average stiffness, average peak load and average separation at failure of the experimental data.

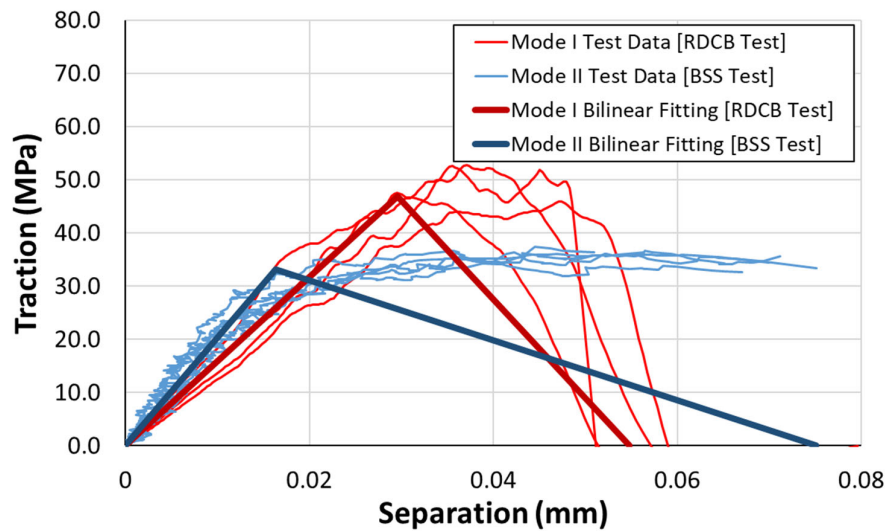


Figure 6. Cohesive traction-separation relationship in Mode I and Mode II for the BetaGuard CI6125R adhesive.

Table 3. Cohesive zone characterization parameters for the BetaGuard CI6125R adhesive

Loading Direction	Stiffness (MPa/mm)	Peak Traction (MPa)	Critical Energy Release Rate (kJ/mm²)
Mode I	1582.90 ± 282.24	46.82 ± 3.86	1.28 ± 0.10
Mode II	2027.06 ± 334.88	33.08 ± 1.16	1.24 ± 0.12

3.2. SLJ and CT Adhesive Joint Testing

The force-displacement response (Figure 7) of the SLJ (red, light blue, and light green curves), 0° CT (darker shades of red, blue and green curves), 45° CT (yellow curve) and 90° CT (black, grey and light grey curves) showed good repeatability and low variability in terms of stiffness and peak load (highest standard deviation among all datasets was 7.9% relative to the mean) (Table 4). The SLJ and CT joints exhibited some variability in the displacement at failure, which was more pronounced in 1 mm Al symmetrical joints regardless of loading angle. The variability in the displacement at failure of SLJ and 90° CT was attributed to the substantial yielding in the 1 mm thick Al, which affected the geometry of the specimen (bending, stretching and width reduction). The 0° CT exhibited bending stresses at the edges of the grip areas, which caused plastic deformation in the 1 mm adherends.

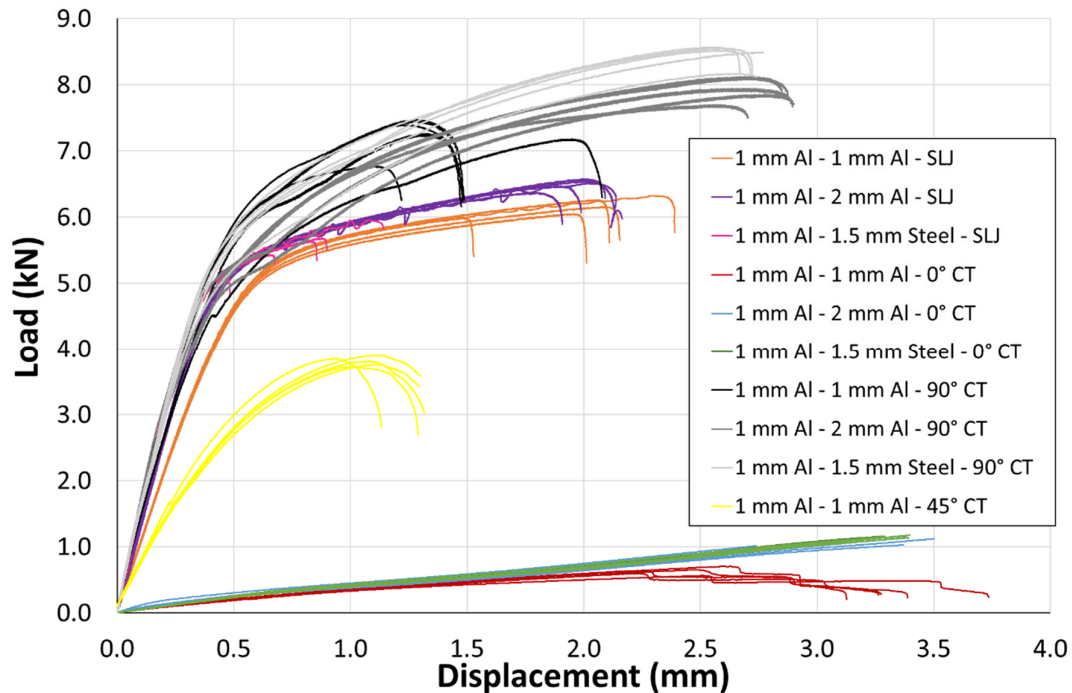


Figure 7. Load-displacement response for SLJ and CT joints under 0°, 45° and 90° loading.

Table 4 Peak load and displacement at failure values for the tested specimens

Test	Material Combination	Thickness Combination (mm)	Average Peak Load (kN)	Average Displacement at Failure (mm)
SLJ			6.16 ± 0.14	2.03 ± 0.31
CT 0°	Al - Al	1 + 1	0.63 ± 0.05	3.35 ± 0.29
CT 45°			4.01 ± 0.06	1.26 ± 0.07
CT 90°			7.22 ± 0.27	1.55 ± 0.30
SLJ	Al - Al	1 + 2	6.50 ± 0.07	2.05 ± 0.10
CT 0°			1.08 ± 0.06	3.24 ± 0.29
CT 90°			7.95 ± 0.17	2.84 ± 0.08
SLJ	Al - Steel	1 + 1.5	5.56 ± 0.31	0.81 ± 0.24
CT 0°			1.15 ± 0.01	3.33 ± 0.05
CT 90°			8.46 ± 0.16	2.74 ± 0.03

3.2.1. SLJ Tests

The 1 mm Al symmetrical joints had an average peak load of 6.16 kN, and an average displacement at failure of 2.04 mm. The 1 mm Al - 2 mm Al joints had a stiffer response and increased the peak load (+5.5%) to 6.49 kN while maintaining similar displacement at failure.

The 1 mm Al - 1.5 mm steel joints had the highest initial stiffness; however, the peak load

dropped, relative to the 1 mm symmetrical joints, to 5.56 kN (-9.6%). The joints exhibited an early displacement at failure of 0.81 mm (-60.1% lower than the 1 mm symmetrical joints) with higher relative variability (± 0.24 mm, $\pm 25.6\%$), although in-line with the magnitude of variability of the aluminum only-cases (up to ± 0.31 mm). The deformation characteristics of the adherends highly influenced the joint response of SLJ tests. Both the symmetrical and asymmetrical SLJ joints exhibited localized joint rotation within the joint overlap region and bending deformation of the adherend varied in each joint (Figure 8). The adhesive layer was subjected to varying degrees of mixed mode loading due to varying degrees of adherend bending near the free ends of the adhesive, initiating an adhesive crack at the ends of the bond line then propagating toward the center.

Changing the sheet thickness and material type of the adherend added loading eccentricity while influencing the material yield strength and flexural stiffness (stiffness of material when subjected to bending), which could be calculated using the modulus of elasticity and second moment of area. Measuring joint rotation during the SLJ tests facilitated quantifying the bending deformation. The SLJ joint with 1 mm Al adherends failed at a rotation angle of about 6 degrees (Figure 8). The asymmetrical joints with 2 mm Al or 1.5 mm steel adherends had higher flexural stiffness (8 - 10 times higher than the 1 mm Al) due to the increase in moment of inertia (Al) or increase in modulus of elasticity (steel). The 2 mm Al and 1.5 mm steel adherends had comparable flexural stiffness (i.e., the higher modulus of elasticity of steel compensated for the lower sheet thickness); however, the joints with the steel adherend failed earlier at a lower peak load and joint rotation (magenta curves, Figure 8). The rotation angle measurements confirmed that the 1 mm Al - 1.5 mm steel joints did not fail prematurely due to higher bending deformations. Contrary to the common examples on symmetrical joints from the literature showing an increase in joint strength with higher strength adherends [12],

the results of this study showed that asymmetrical joints may not follow a similar trend. During elastic loading of 1 mm Al – 1.5 steel SLJ, the whole length of the adhesive was involved in transferring the load causing global yielding within the adhesive [14]; however, the stiffer steel adherend with higher yield strength limited the joint rotation (Figure 8, green curve) as steel resisted bending, which resulted in localized shear strains within the 1 mm aluminum adherend and adhesive layer. The low ductility of the adhesive increased the localized shear strain regions near the free ends of the adhesive [14], resulting in lower joint strength and higher variability in the displacement to failure values (Table 4). Also, the higher stiffness ratio between adherends increased the maximum principal stress at the mid-section of the adhesive [27]. SLJ joint strengths for symmetrical joints made with Al (AA5182 alloy with Young’s modulus of 70 GPa and YS of 170 MPa) were 5.9% higher than the joint strengths of asymmetrical joints made with the same Al alloy and ultra-high-strength steel (Usibor® with Young’s modulus of 200 GPa and YS of 1100 MPa) [1]. Importantly, adhesively joined SLJ made with two dissimilar materials of a substantial difference in elastic modulus and strength can exhibit localized strains within the lower strength, more flexible adherend, which can extend to the free ends of the adhesive layer. For low ductility adhesives, the localized strains will initiate a crack and reduce joint strength relative to symmetrical joints.

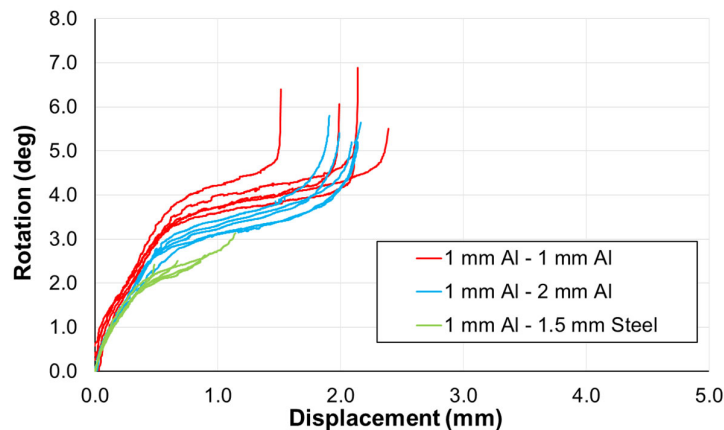


Figure 8. Rotation-displacement response for SLJ joints made with 1 mm Al - 1 mm Al, 1 mm Al - 2 mm Al and 1 mm Al - 1.5 mm steel.

3.2.2. 0° CT Tests

The 1 mm symmetrical 0° CT tests had an average peak load of 0.63 kN, and an average displacement at failure of 3.35 mm. The 1-2 mm joints had a stiffer response and increased the peak load (+71.2%) to 1.08 kN while maintaining similar displacement at failure. Comparing the joints with 1.5 mm steel and 2 mm Al adherends, the former showed similar initial stiffness, slightly higher peak load (+6.5%) and similar displacement at failure (2.7% difference). The displacement at failure of the 1 mm symmetrical 0° CT was the highest of all configurations tested (63.4%, 161.7% and 116.1% higher than similar SLJ, 45° CT and 90° CT specimens, respectively). Also, it was clear from the force-displacement response (dark red lines, Figure 7) that the peak load corresponded to the adhesive damage initiation; however, the joint did not fail abruptly. The symmetrical joints showed multiple crack arrests attributed to the progressive adherend bending. When the thickness or yield strength of the adherend materials was increased, the overall specimen compliance and bending deformations decreased, increasing joint strength.

The results suggested that material strength and sheet thickness inversely correlated with the compliance of adhesive joined CT specimens, which increased joint strength under Mode I loading. The adhesive was subjected to peeling forces at the bond line boundaries due to the bending deformations in the loaded and fixed adherends. Other studies have reported that adhesive CT specimens with Al adherends demonstrated large displacement at failure (~6.7 mm) and post-failure images of specimens showed significant adherend bending [18].

3.2.3. 45° CT Tests

The 45° CT tests exhibited an average peak load of 4.01 kN and an average displacement at failure of 1.28 mm. During the test, the adhesive was subjected to mixed-mode loading and

showed limited adherend bending deformations. The adherends exhibited substantially lower bending deformations and test specimen compliance relative to 0° CT, which reduced the peel loading at the adhesive boundaries. As a result, the joint peak load was higher than the 0° CT (+536.5%) but lower than the peak load of similar SLJ (-34.9%) and 90° CT (-44.4%) tests. The displacement at failure for this test specimen was the lowest (1.28 mm) among all tests, indicating that the CT specimen compliance was highly sensitive to the loading angle.

3.2.4. 90° CT Tests

The 90° CT test loaded the adhesive joint in shear with the load parallel to the adherend width (Figure 4d), as opposed to SLJ joints which had the shear loading parallel to the adhesive layer length. This loading orientation had somewhat limited attention in previous studies, but it offered an additional validation case for the FE modelling approach. Interestingly, the maximum average peak load was exhibited by the 90° CT with the load applied in the second shear direction of adhesive. Similar SLJ joints showed lower joint strength (-14.7% difference), indicating that the 90° CT configuration might have reduced the peel stresses at the adhesive edge by limiting the joint rotation. Because the CT geometry offered limited access to optically measure joint rotation, the deflection of the adherends and stresses within the adhesive layer were analyzed using the FE simulation results to quantify the peel stresses at the adhesive boundaries (section 3.3.4. 90° CT Model Results and Validation). Also, this test benefited from asymmetrical joining with higher adherend thickness or material strength achieving up to 17.1% higher peak compared to 1 mm Al – 1 mm Al joints.

3.2.5. Joint Comparison

A statistical analyses package (SPSS Statistics 28, IBM) was used to carry out a statistical analysis on the data using two-way Analysis of Variance (ANOVA) with Tukey posthoc analysis for pair-wise comparisons. The peak load data for the SLJ, 0° CT, 45° CT and 90° CT tests showed statistically significant differences ($p < 0.05$) and joint asymmetry had a significant influence on the peak load of the adhesive joint for all types of tests. The adhesive joint strength generally correlated with adherend thickness and material strength (Pearson's and Spearman's correlation coefficients > 0.5), except for the SLJ tests which suffered premature failure for the 1 mm Al - 1.5 mm Steel. Adhesive joint strength also correlated with the loading angle of CT tests.

The fracture surface for each test showed distinct characteristics with the fracture generally propagating within the adhesive layer close to the interface of one adherend. For SLJ specimens, the crack initiated at the leading and trailing edges of the adhesive close to the interface and the crack path progressed from both ends along the bond line length toward the center, which resulted in a sharp transition zone near the centre line of the bond line length (Figure 9a). For CT specimens, the fracture surfaces changed in shape and edge characteristics. One of the limitations of the CT specimen was that it did not offer visual access to the bond line thickness, which made it challenging to confirm the crack initiation location using optical techniques. The 0 deg CT failure surface indicated that the central zone of the bonding area and the adhesive boundaries controlled the damage initiation and progression (Figure 9b). The 45 deg CT failure surface was relatively similar to the SLJ with more hackles at the transition line and a shift in the transition line between the central region and the edges (Figure 9c). The failure surface could indicate that the adhesive damage initiation was similar to the SLJ specimens but the further extent of mode mixity affected the crack progression at

the free ends, shifting the transition zone from the center of the adhesive layer length. The 90 deg CT failure surface indicated that the leading adhesive boundary exhibited edge effects different than the trailing boundary (Figure 9d). The leading boundary exhibited in-plane compression load while the trailing boundary exhibited in-plane tension as the joint rotated.

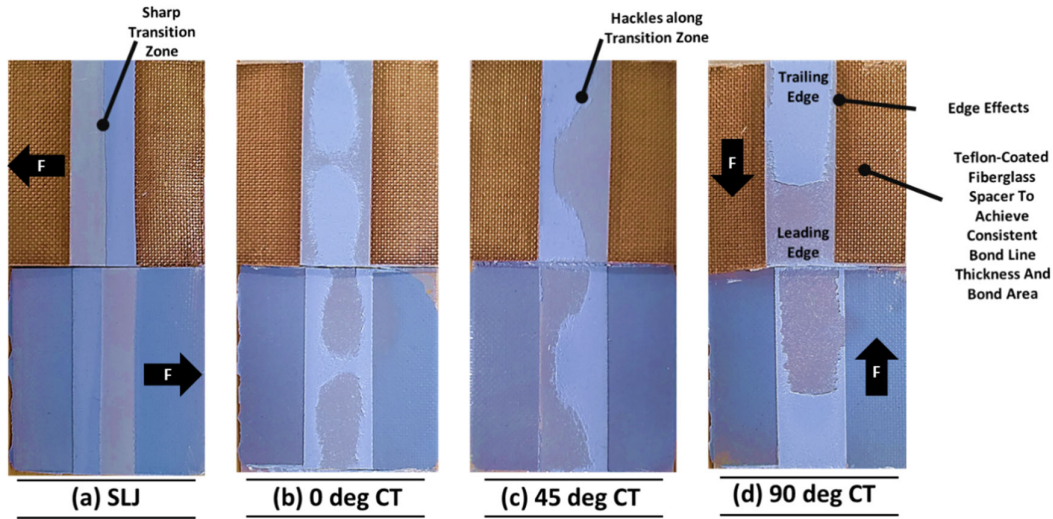


Figure 9. Fracture surfaces of SLJ (a) and CT joints under 0 deg (b), 45 deg (c) and 90 deg (d) loading. (F indicates the load orientation)

3.3. Finite Element Model Validation

3.3.1. SLJ Model Results and Validation

The SLJ simulation results showed good agreement with the initial stiffness and peak load (<10% difference) with somewhat larger displacement at failure (<30% difference) (Figure 10a and b). In the linear loading region, the response of the FE models was somewhat stiffer due to the intrinsically stiff behaviour of fully integrated shell elements, attributed to the number of integration points in-plane. The models captured the adherend bending deformation and the SLJ joint rotation, mimicking the local joint kinematics and mixed-mode loading at the adhesive free ends (Figure 11). The overprediction of displacement at failure was observed in other studies using thin aluminum adherends [1], and could be more relevant to adherend

deformation than CZM response. Prior to adhesive failure, the 1 mm Al adherend exhibited yielding in all SLJ configurations with plastic deformation in the form of adherend stretching and width reduction. The plastic deformation of the 1 mm Al adherend reduced further adherend bending (*i.e.* joint rotation) and consequently reduced Mode I loading at the adhesive free ends. The FE model showed higher in-plane plastic deformation compared to the experiments, with a 1 mm Al adherend width reduction of up to 0.9 mm compared to up to 0.65 mm in experiments. The higher width reduction in FE models led to over predicting the joint displacement at failure.

The joint rotation measurements from the SLJ tests were compared to the simulation results (Figure 10c and d). The FE models of the SLJ joint captured the adherend bending deformation and joint rotation, mimicking the local joint kinematics and mixed-mode loading at the adhesive free ends (Figure 11). The use of the optical measurements and extracting the nodal coordinates corresponding to the optically tracked points on the side of the SLJ specimen, served as a validation metric while limiting the influence of the test setup (e.g., frame compliance) and in-plane deformations of the adherends (e.g., adherend stretching). The effect of loading eccentricity in asymmetrical joints was captured using shell elements. The sharp increase in rotation angle corresponded to the rapid progression of adhesive damage prior to joint separation, and the change in the rate of rotation (slope change near the 2° rotation) corresponded to adherend yielding on-set.

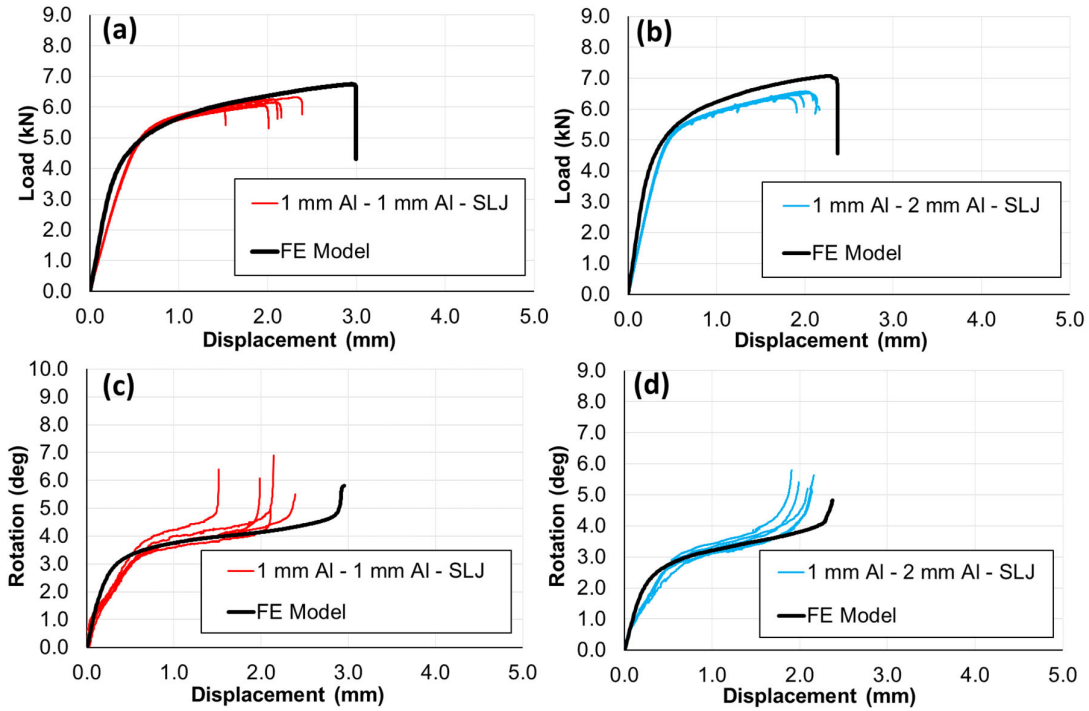


Figure 10. FE model validation for SLJ models, comparing the load-displacement and joint rotation responses of symmetrical (a, c) and asymmetrical (b, d) tests.

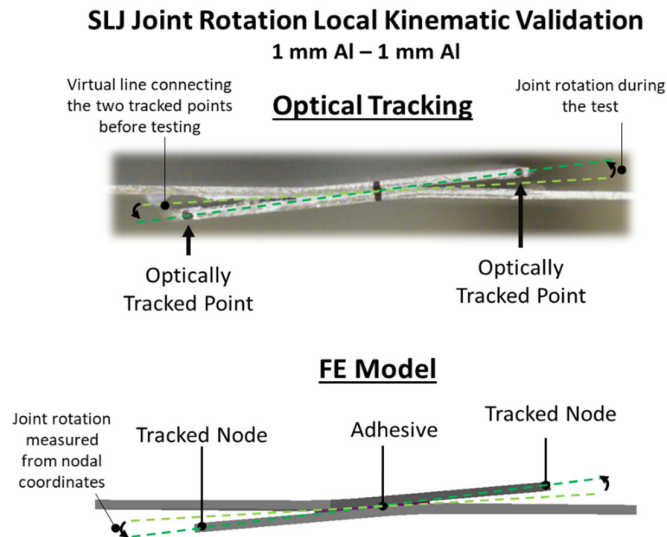


Figure 11. The joint rotation validation using the optical measurements from experimental testing and node coordinates tracking from the FE model prediction.

3.3.2. 0° CT Model Results and Validation

The 0° CT model (Figure 5b) response showed good agreement with initial stiffness, peak load (<15% difference), and captured the damage initiation of the symmetrical and asymmetrical joints (Figure 12a, b and c). The stiffness response was somewhat over-predicted at higher

loads as the localized bending of shell elements and reduced geometry compliance at higher displacement stiffened the response (i.e., numerical stiffening effect). The unloading behaviour of symmetrical joints with multiple crack arrests could not be captured using the proposed CZM model, which could be attributed to the unloading (softening) behaviour of the traction-separation relationship. According to Park et al. [28], non-potential based cohesive models, in particular the cohesive model available in Abaqus, did not always provide a negative tangent stiffness during the unloading phase, resulting in an unphysical behaviour. In this particular loading condition, the separation increased closer to failure, but traction increased and decreased repeatedly causing numerical instability. Importantly, the stress distribution in the loaded adherend was significantly higher than the fixed one (Figure 12d) regardless of joint symmetry, attributed to the geometry of bonding area resulting in higher bending deformations. Such asymmetrical deformation between the loaded and fixed adherends resulted in adhesive peeling and decreased joint strength.

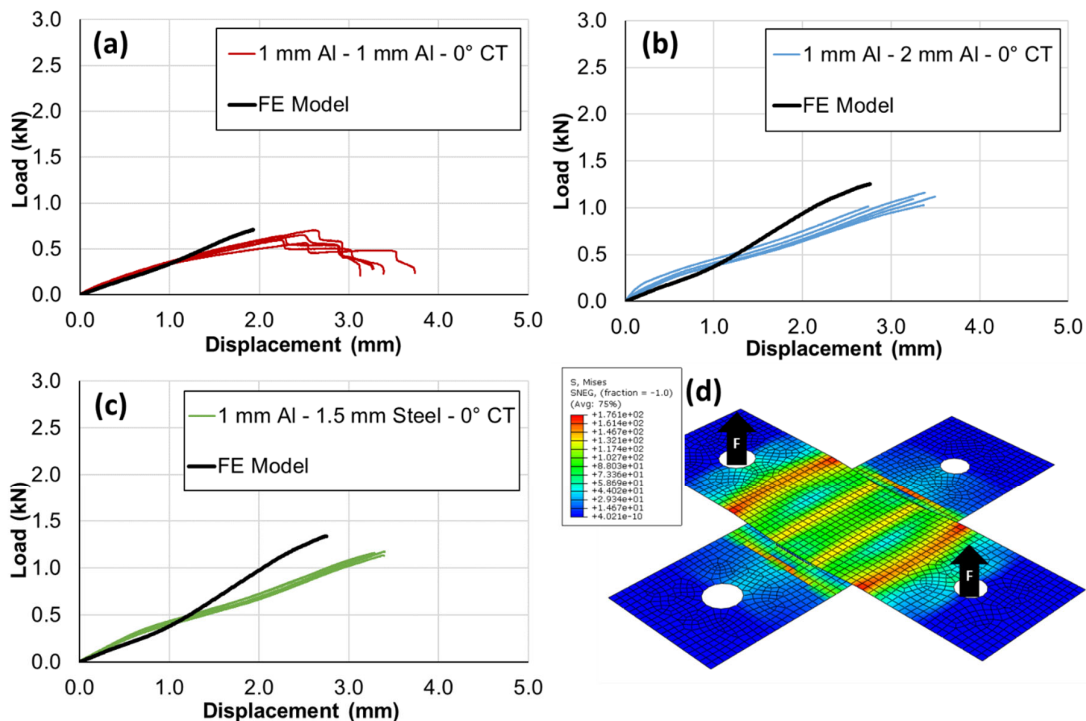


Figure 12. Numerical model validation for and 0° CT joints made with 1 mm Al - 1 mm Al (a), 1 mm Al - 2 mm Al (b) and 1 mm Al - 1.5 mm Steel (c), together with the stress distribution in (a) before adhesive failure.

3.3.3. 45° CT Model Results and Validation

The 1 mm Al – 1 mm Al model under 45° loading angle showed good agreement (<2% difference in peak load) with the experimental data (Figure 13a). The tension loading component resulted in adherend bending and the shear loading component resulted in joint rotation in the adherends. Contrary to the SLJ tests, the rotation at one end was constrained by the fixed adherend; thus, the stresses at the constrained bend region (Constrained Bend Region, Figure 13b) within the loaded adherend were higher (+60%) than the freely rotating bend region (Freely Rotating Bend Region, Figure 13b). The free rotation at the other end facilitated initiating adhesive damage, and the adhesive damage progressed from the corners closer to the freely rotating bend region (Adhesive Damage, Figure 13b). Importantly, the adhesive did not exhibit a uniform mixed-mode loading, but varying degrees of mode mixity.

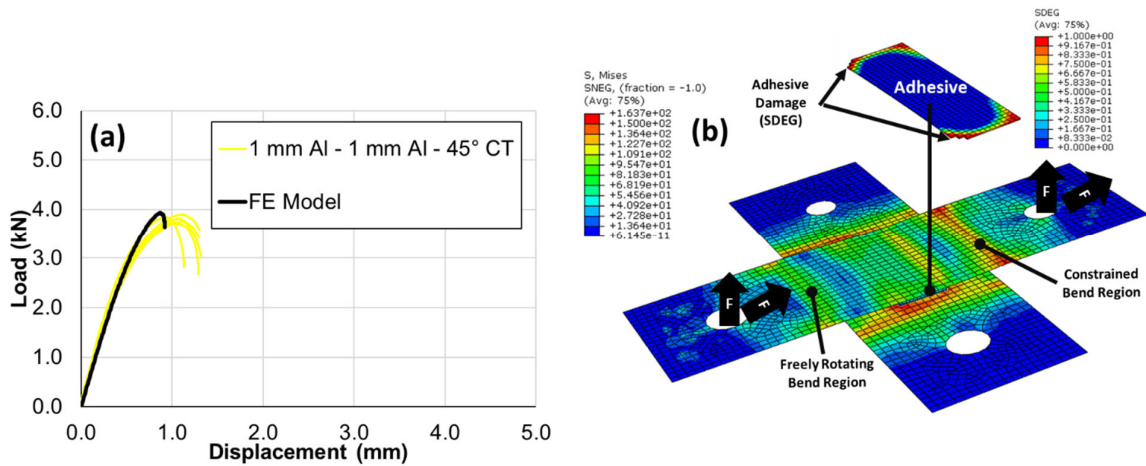


Figure 13. Numerical model validation for the 45° CT joints made with 1 mm - 1 mm Al (a), together with the nodal displacement distribution before adhesive failure (b).

3.3.4. 90° CT Model Results and Validation

The CT models with 90° loading angle (Figure 5b with prescribed displacement parallel to adherend width) showed good agreement with stiffness and somewhat higher peak load prediction (<19% difference) for symmetrical (Figure 14a) and asymmetrical joints (Figure 14b). The displacement at failure could not be measured due to convergence difficulties,

encountered during damage progression due to numerical instability. The numerical instability could be attributed to the effect of solution jump (sudden deformation recovery when CZM traction drops to zero) and high relative stiffness at the interface (the ratio between CZM stiffness and non-linear material stiffness response) [29]. The use of Riks iterative method, viscous regulation method, and quasi-Newton iterative methods were proposed to address similar challenges. Riks and quasi-Newton iterative methods were not adopted because of their effect on solution speed, which makes them undesirable for large models (*e.g.* full-car model) [29]. In this study, viscous regulation helped in improving convergence; however, the approach could not resolve the solution jump, which is usually caused by high material nonlinearity and in-plane and out-of-plane localized deformations at the CZM interface. Further investigation showed substantial in-plane localized compression stress in the adherends (Figure 14c). Also, the loaded adherend rotated while being constrained by the fixed adherend (Figure 14d), which resulted in mixed mode loading with localized tension and compression stresses at the adhesive free ends (Figure 14e). The compression loading under Mode I caused unphysical behaviour of CZM damage propagation (Figure 14f), attributed to the CZM formulation lacking compression loading. In the loaded SLJ, the joint rotated freely around the adhesive joint (Figure 15a) resulting in mixed mode loading with localized peel loading at both free ends of the adhesive. However, the loaded 90° CT joint exhibited constrained rotation which resulted in less mode mixity compared to SLJ joints (Figure 15b). Although this load condition exhibited less mode mixity compared to SLJ joints, the localized compression stresses within the adhesive joint may not be common in structural joints.

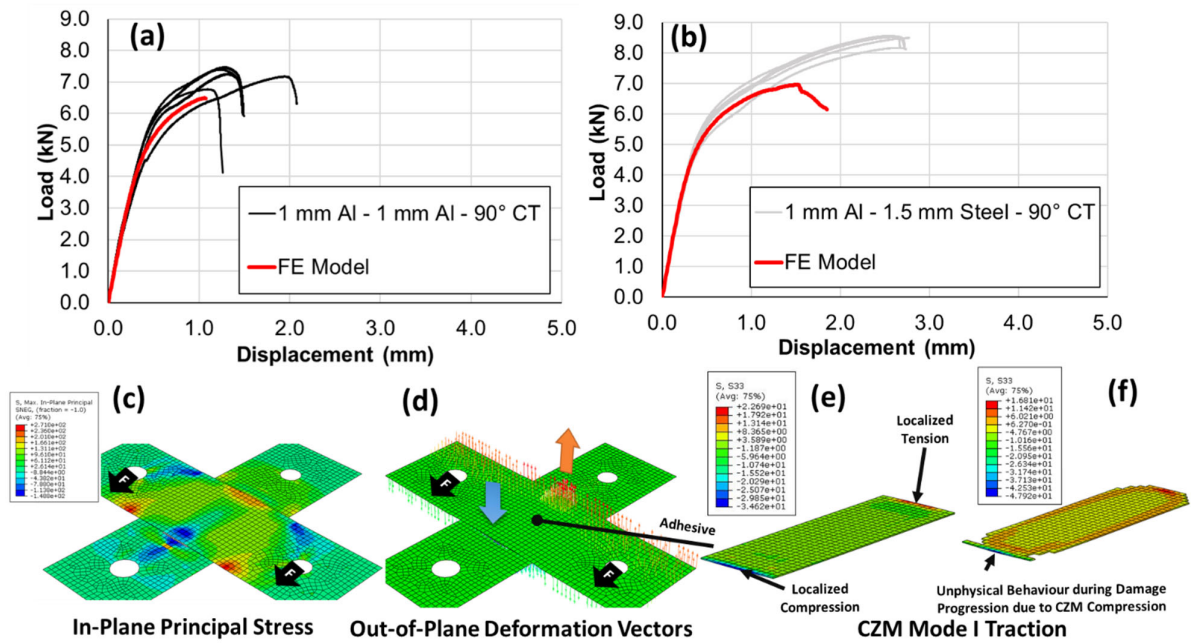


Figure 14. Numerical model validation for the 90° CT joints made with 1 mm - 1 mm Al (a), and 1 mm - 1.5 mm Steel (b) with illustrations of the principal stress distribution (c), out-of-plane deformations (d) and adhesive traction in Mode I (e-f).

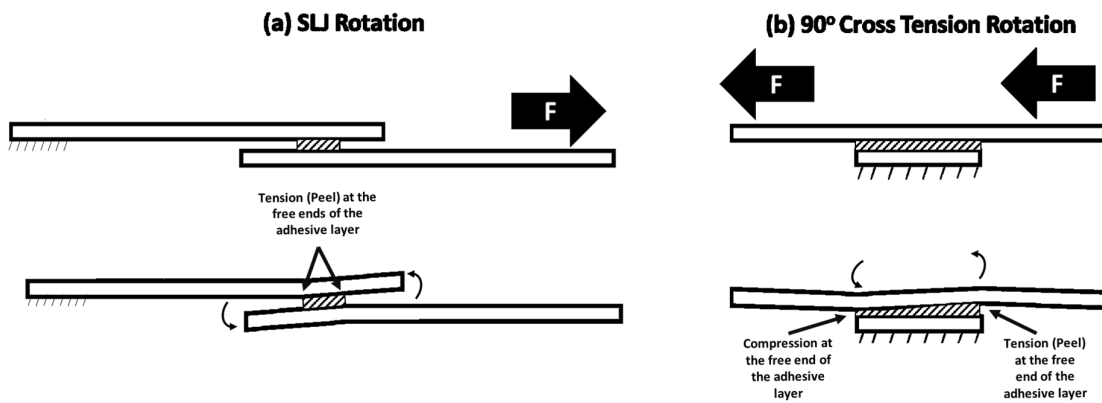


Figure 15. Joint rotation in loaded SLJ (a) and 90° CT (b) tests.

4. Conclusion

The material-level adhesive characterization, using RDCB and BSS specimens, enabled the determination of the CZM parameters with fewer tests relative to traditional approaches, allowing for the modeling of adhesive joints with complex deformations and modes of loading. Asymmetrical joining showed a statistically significant ($p < 0.05$) influence on

adhesive joints for all types of tests, with joint strength improvement depending on the test specimen geometry and the deformations in the thinner adherend. The 0° CT and 90° CT tests showed that asymmetrical joints, made with higher adherend thickness or material strength, exhibited improved joint strength (up to 82.5% and up to 17.1%, respectively) relative to symmetrical joints with 1 mm aluminum adherends. In contrast, the 1 mm Al – 2 mm Al SLJ joints exhibited modest strength improvement relative to symmetrical joints (+5.5%), and the joints with the steel adherend failed earlier at a lower peak load (-9.6%), attributed to the localized shear strains within the 1 mm aluminum adherend and adhesive layer. The fracture surfaces showed distinct characteristics depending on the test specimen and mode of loading. The FE modeling methodology, incorporating the CZM method and shell elements with a surface-to-surface tied constraint, is compatible with large-scale models needed in the automotive industry, facilitating efficient modeling of future adhesive joined structures. The FE models were validated using the force-displacement response and local joint kinematics for symmetric and asymmetric joints under various modes of loading, including assessment of joint bending deformations, stress distribution, and adhesive damage initiation in SLJ and CT joints. The simulation results highlighted some joint-specific limitations related to capturing the adhesive crack progression using CZM, such as the displacement at failure of SLJ joints, and numerical instability of 90° CT tests. The 45° CT simulation results suggested that the adhesive did not experience uniform mode mixity, attributed to the constrained joint rotation.

Overall, joint asymmetry had a significant influence on the peak load and displacement at failure of the adhesive joints. Material-level adhesive characterization and adhesive joint FE modeling, using CZM and shell elements, predicted the responses of a variety of test specimens with complex adherend deformation and modes of loading.

Acknowledgement

The authors would like to express their thanks to Renault Group for their financial support of this research.

5. References

- [1] Watson B, Nandwani Y, Worswick MJ, Cronin DS. Metallic multi-material adhesive joint testing and modeling for vehicle lightweighting. *Int J Adhes Adhes* 2019;95:102421. <https://doi.org/10.1016/j.ijadhadh.2019.102421>.
- [2] Lanzerath H, Pasligh N. Benefit of Structural Adhesives in Full Car Crash Applications. *SAE Tech Pap* 2014;2014-01-08. <https://doi.org/10.4271/2014-01-0811>.
- [3] dos Reis MQ, Banea MD, da Silva LFM, Carbas RJC. Mechanical characterization of a modern epoxy adhesive for automotive industry. *J Brazilian Soc Mech Sci Eng* 2019;41:1-11. <https://doi.org/10.1007/s40430-019-1844-2>.
- [4] da Silva LFM, Öchsner A, Adams RD. *Handbook of Adhesion Technology: Second Edition*. vol. 1-2. Springer Heidelberg; 2018. <https://doi.org/10.1007/978-3-319-55411-2>.
- [5] Ezzine MC, Amiri A, Tarfaoui M, Madani K. Damage of bonded, riveted and hybrid (bonded/riveted) joints, Experimental and numerical study using CZM and XFEM methods. *Adv Aircr Spacecr Sci* 2018;5:595-613. <https://doi.org/10.12989/aas.2018.5.5.595>.
- [6] Weiland J, Debruyne S, Vandepitte D, Pulm M, Schiebahn A, Reisgen U. Stiffness and strength analysis of hybrid adhesive bonded-resistance spot welded sandwich samples by means of virtual FE testing. *J Adhes* 2019;95:543-57. <https://doi.org/10.1080/00218464.2018.1553713>.
- [7] Khayer Dastjerdi A, Tan E, Barthelat F. Direct Measurement of the Cohesive Law of Adhesives Using a Rigid Double Cantilever Beam Technique. *Exp Mech* 2013;53:1763-72. <https://doi.org/10.1007/s11340-013-9755-0>.
- [8] Watson B, Liao CH, Worswick MJ, Cronin DS. Mode I traction-separation measured using rigid double cantilever beam applied to structural adhesive. *J Adhes* 2018;96:717-37. <https://doi.org/10.1080/00218464.2018.1502666>.
- [9] Watson B, Worswick MJ, Cronin DS. Quantification of mixed mode loading and bond line thickness on adhesive joint strength using novel test specimen geometry. *Int J Adhes Adhes* 2020;102:102682. <https://doi.org/10.1016/j.ijadhadh.2020.102682>.
- [10] Machado JJM, Marques EAS, Silva MRG, da Silva LFM. Numerical study of impact behaviour of mixed adhesive single lap joints for the automotive industry. *Int J Adhes Adhes* 2018;84:92-100. <https://doi.org/10.1016/j.ijadhadh.2018.02.036>.
- [11] Di Franco G, Fratini L, Pasta A. Analysis of the mechanical performance of hybrid

- (SPR/bonded) single-lap joints between CFRP panels and aluminum blanks. *Int J Adhes Adhes* 2013;41:24–32. <https://doi.org/10.1016/j.ijadhadh.2012.10.008>.
- [12] da Silva LFM, Carbas RJC, Critchlow GW, Figueiredo MAV, Brown K. Effect of material, geometry, surface treatment and environment on the shear strength of single lap joints. *Int J Adhes Adhes* 2009;29:621–32. <https://doi.org/10.1016/j.ijadhadh.2009.02.012>.
- [13] Ibrahim AH, Cronin DS. Mechanical testing of adhesive, self-piercing rivet, and hybrid jointed aluminum under tension loading. *Int J Adhes Adhes* 2022;113:103066. <https://doi.org/10.1016/j.ijadhadh.2021.103066>.
- [14] Karachalios EF, Adams RD, da Silva LFM. Single lap joints loaded in tension with high strength steel adherends. *Int J Adhes Adhes* 2013;43:81–95. <https://doi.org/10.1016/j.ijadhadh.2013.01.016>.
- [15] Karachalios EF, Adams RD, da Silva LFM. Single lap joints loaded in tension with ductile steel adherends. *Int J Adhes Adhes* 2013;43:96–108. <https://doi.org/10.1016/j.ijadhadh.2013.01.017>.
- [16] Ciardiello R, Greco L, Miranda M, Sciuolo F Di, Goglio L. Experimental investigation on adhesively bonded U-shaped metallic joints using the Arcan test. *J Adv Join Process* 2020;1:100010. <https://doi.org/10.1016/j.jajp.2020.100010>.
- [17] Terasaki N, Fujio Y, Horiuchi S, Akiyama H, Itabashi M. The Journal of Adhesion ISSN: (Print) (Online) Journal homepage: <https://www.tandfonline.com/loi/gadh20> Mechanoluminescent study for optimization of joint design on cross tension test Mechanoluminescent study for optimization of joint design on cross tension test 2021. <https://doi.org/10.1080/00218464.2021.2009807>.
- [18] Ufferman B, Abke T, Barker M, Vivek A, Daehn GS. Mechanical properties of joints in 5052 aluminum made with adhesive bonding and mechanical fasteners. *Int J Adhes Adhes* 2018;83:96–102. <https://doi.org/10.1016/j.ijadhadh.2018.02.030>.
- [19] Boutar Y, Naïmi S, Mezlini S, Ali MBS. Effect of surface treatment on the shear strength of aluminium adhesive single-lap joints for automotive applications. *Int J Adhes Adhes* 2016;67:38–43. <https://doi.org/10.1016/j.ijadhadh.2015.12.023>.
- [20] Sousa FC, Akhavan-Safar A, Goyal R, da Silva LFM. The influence of mode mixity and adhesive system on the fatigue life of adhesive joints. *Fatigue Fract Eng Mater Struct* 2020;43:2337–48. <https://doi.org/10.1111/ffe.13301>.
- [21] Zhang J, Wang J, Yuan Z, Jia H. Effect of the cohesive law shape on the modelling of adhesive joints bonded with brittle and ductile adhesives. *Int J Adhes Adhes* 2018;85:37–43. <https://doi.org/10.1016/j.ijadhadh.2018.05.017>.
- [22] Fernandes TAB, Campilho RDSG, Banea MD, Da Silva LFM. Adhesive selection for single lap bonded joints: Experimentation and advanced techniques for strength prediction. *J Adhes* 2015;91:841–62. <https://doi.org/10.1080/00218464.2014.994703>.
- [23] Akhavan-Safar A, Monteiro J, Carbas R, Marques E, Goyal R, da Silva LFM. Tensile fatigue life prediction of adhesively bonded structures based on CZM technique and a

modified degradation approach. Proc Inst Mech Eng Part G J Aerosp Eng 2020;234:1988–99. <https://doi.org/10.1177/0954410020951675>.

- [24] Campilho RDSG, de Moura MFSF, Domingues JJMS. Numerical prediction on the tensile residual strength of repaired CFRP under different geometric changes. Int J Adhes Adhes 2009;29:195–205. <https://doi.org/10.1016/j.ijadhadh.2008.03.005>.
- [25] Marzi S, Hesebeck O, Brede M, Kleiner F. A Rate-Dependent, Elasto-Plastic Cohesive Zone Mixed-Mode Model for Crash Analysis of Adhesively Bonded Joints. 7th Eur LS-Dyna Conf 2009.
- [26] Alfano M, Furgiuele F, Leonardi A, Maletta C, Paulino GH. Cohesive Zone Modeling of Mode I Fracture in Adhesive Bonded Joints. Key Eng Mater 2007;348–349:13–6. <https://doi.org/10.4028/www.scientific.net/kem.348-349.13>.
- [27] Reis PNB, Ferreira JAM, Antunes F. Effect of adherends rigidity on the shear strength of single lap adhesive joints. Int J Adhes Adhes 2011;31:193–201. <https://doi.org/10.1016/j.ijadhadh.2010.12.003>.
- [28] Park K, Choi H, Paulino GH. Assessment of cohesive traction-separation relationships in ABAQUS: A comparative study. Mech Res Commun 2016;78:71–8. <https://doi.org/10.1016/j.mechrescom.2016.09.004>.
- [29] Sepasdar R, Shakiba M. Overcoming the convergence difficulty of cohesive zone models through a Newton-Raphson modification technique. Eng Fract Mech 2020;233. <https://doi.org/10.1016/j.engfracmech.2020.107046>.